Check for updates



OCEANOGRAPHY

Oceanic uptake of CO₂ enhanced by mesoscale eddies

Xueyin Li¹, Bolan Gan^{1,2}*, Zhengguang Zhang^{1,2}, Zhimian Cao³, Bo Qiu⁴, Zhaohui Chen^{1,2}, Lixin Wu^{1,5}

Oceanic mesoscale eddies play a crucial but underexplored role in regulating carbon fluxes and climate change. While they redistribute heat, salt, nutrients, and other tracers, their effects on CO₂ uptake remain uncertain. Using observation-based machine learning to estimate CO₂ fluxes throughout the lifetimes of thousands of eddies, we show that anticyclonic eddies substantially enhance CO₂ uptake on average, while cyclonic eddies marginally diminish it. This asymmetry yields an overall net increase in CO_2 absorption by 9.98 \pm 2.28 and 13.82 \pm 9.94% in the Kuroshio Extension and Gulf Stream, respectively, major carbon sequestration regions. The primary driver of this enhanced uptake is the downward pumping of dissolved inorganic carbon within anticyclonic eddies. Asymmetric biological responses between anticyclonic and cyclonic eddies contribute to the overall eddy-induced CO2 flux imbalance. The finding suggests a potential underestimation of the ocean's capacity for carbon sequestration because of insufficient incorporation of eddies in current observations, emphasizing the need for expanded monitoring in eddy-rich, undersampled regions.

Copyright @ 2025 The Authors, some rights reserved; exclusive licensee American Association for the Advancement of Science. No claim to original U.S. Government Works. Distributed under a Creative Commons Attribution NonCommercial License 4.0 (CC BY-NC).

INTRODUCTION

The past few decades have witnessed a rapid accumulation of carbon dioxide (CO₂) in the atmosphere, serving as one of the primary catalysts for global warming and numerous extreme events (1-3). The latest global carbon budget over 2013 to 2022 estimates that the ocean annually absorbs ~26% of anthropogenic CO₂ emissions (more than 2000 megatons of carbon) through CO₂ flux (FCO₂) at the surface, demonstrating an indispensable role of the ocean in climate change mitigation (4).

Precise estimation of ocean carbon sink is essential in determining the global carbon budget and evaluating the remaining carbon budgets available to humanity (5, 6). However, considerable uncertainties persist in these calculations (4, 5). For instance, an uncertainty of ± 0.9 Pg C year⁻¹ represents ~56% of the total estimated ocean carbon sink (-1.6 Pg C year⁻¹) during 1970 to 2007 (2). Moreover, notable discrepancies exist among the estimations of ocean carbon sink over 2013 to 2022 derived from various global ocean biogeochemistry models (4). This issue may arise from variations in their methodologies for calculating sea-air FCO₂, such as gas-exchange parameterization and wind products used, as well as inherent limitations within the underlying dynamic frameworks that describe the interactions between physical processes and ocean ecology and carbon chemistry (7-10). For instance, current global ocean biogeochemistry models and observation-based sea surface partial pressure of CO₂ (pCO₂) products struggle to resolve mesoscale processes (4, 11, 12), including prevalent coherent eddies that play a substantial role in biogeochemical dynamics (13, 14).

Mesoscale eddies, characterized by horizontal scales of O(100 km), are ubiquitous in the global ocean, accounting for nearly 90% of oceanic kinetic energy (13, 15). These eddies exert notable effects comparable to large-scale circulation on the transport and redistribution

of various tracers, substantially influencing nutrient availability and biological production (16-19). They also substantially influence airsea heat flux, causing anomalies on the order of magnitude (~10 to 20 W m⁻²) in eddy-rich regions, as the amplitude of the large-scale annual cycle (20). Despite their widespread distribution and crucial significance, only a limited body of research has explored the modification of mesoscale eddies on sea-air FCO₂ and the ocean carbon sink (21-24). In particular, there are very few case studies using in situ data from onboard sampling, which have suggested divergent results because of a complex balance between solubility and biogeochemical effects of eddies (22, 25-28).

Ideally, anticyclonic eddies with a warm core could increase sea surface pCO₂ through solubility effects, leading to less CO₂ drawdown (29). In the meantime, the biological activity within anticyclonic eddies may be hypothetically suppressed because of reduced nutrient supplies caused by downward displacement of isopycnals, leading to less biological CO₂ uptake (30, 31). Conversely, cyclonic eddies with a cold core could exhibit an opposite pattern (30, 31). In this scenario, anticyclonic eddies may potentially act as weak CO₂ sinks or even sources of CO₂ to the atmosphere, while cyclonic eddies may amplify the CO₂ uptake. These opposing effects of anticyclonic and cyclonic eddies, if symmetrically balanced, could ultimately lead to a nearly negligible net impact on the ocean carbon sink. However, observational studies reveal a more complex relationship, underscoring dissolved inorganic carbon (DIC) as a critical modulator of sea-air FCO₂ (22–28). For instance, anticyclonic eddies have been observed to enhance oceanic CO₂ uptake via surface DIC depletion (22), while a cold-core cyclonic eddy was found to diminish CO₂ uptake by elevating DIC relative to surrounding waters (25). The impact of eddies on sea-air FCO₂ also varies seasonally (23) and regionally (32). Those findings contradict the eddy modulation on FCO₂ that is driven solely by thermal and biological processes, highlighting the complexity of eddy effects on CO₂ uptake. Nevertheless, because of the sparse spatial and temporal coverages of observations that pose substantial challenges in generating continuous highresolution data (8, 33), the net effects of mesoscale eddies on oceanic CO₂ uptake remain unknown.

In a global perspective, the most pronounced ocean sinks for atmospheric CO₂ primarily reside in the confluence regions of the western

¹Frontier Science Center for Deep Ocean Multispheres and Earth System (FDOMES) and Physical Oceanography Laboratory/Academy of Future Ocean, Ocean University of China, Qingdao, China. ²Laboratory for Ocean Dynamics and Climate, Qingdao Marine Science and Technology Center, Qingdao, China. ³State Key Laboratory of Marine Environmental Science, Xiamen University, Xiamen, China. ⁴Department of Oceanography, University of Hawaii at Manoa, Honolulu, HI, USA. 5 Laoshan Laboratory, Qinqdao, China.

^{*}Corresponding author. Email: gbl0203@ouc.edu.cn

boundary currents (WBCs) (2) (Fig. 1A). These regions concurrently exhibit vigorous and prevalent mesoscale eddy activities (Fig. 1B), making it challenging to obtain an accurate observation of their sea-air FCO₂. Among these regions, the Kuroshio Extension (KE) region is where the largest amount of seawater pCO₂ observations is archived (Fig. 1C and fig. S1A). The high frequency of mesoscale eddy activity in this region, coupled with the extensive observational data available, presents a unique opportunity to investigate the net contributions of

anticyclonic and cyclonic eddies to ocean CO_2 sinks. Here, by using both satellite products and observational p CO_2 data spanning from July 2002 to December 2021, combined with machine learning techniques, we have tracked thousands of total anticyclonic and cyclonic eddies (with lifespans over 12 weeks) in the KE region and reconstructed the associated sea-air FCO_2 . On the basis of such a large ensemble, we find a substantial net uptake of CO_2 by eddies, exhibiting an asymmetric pattern with an unexpected higher increase in CO_2

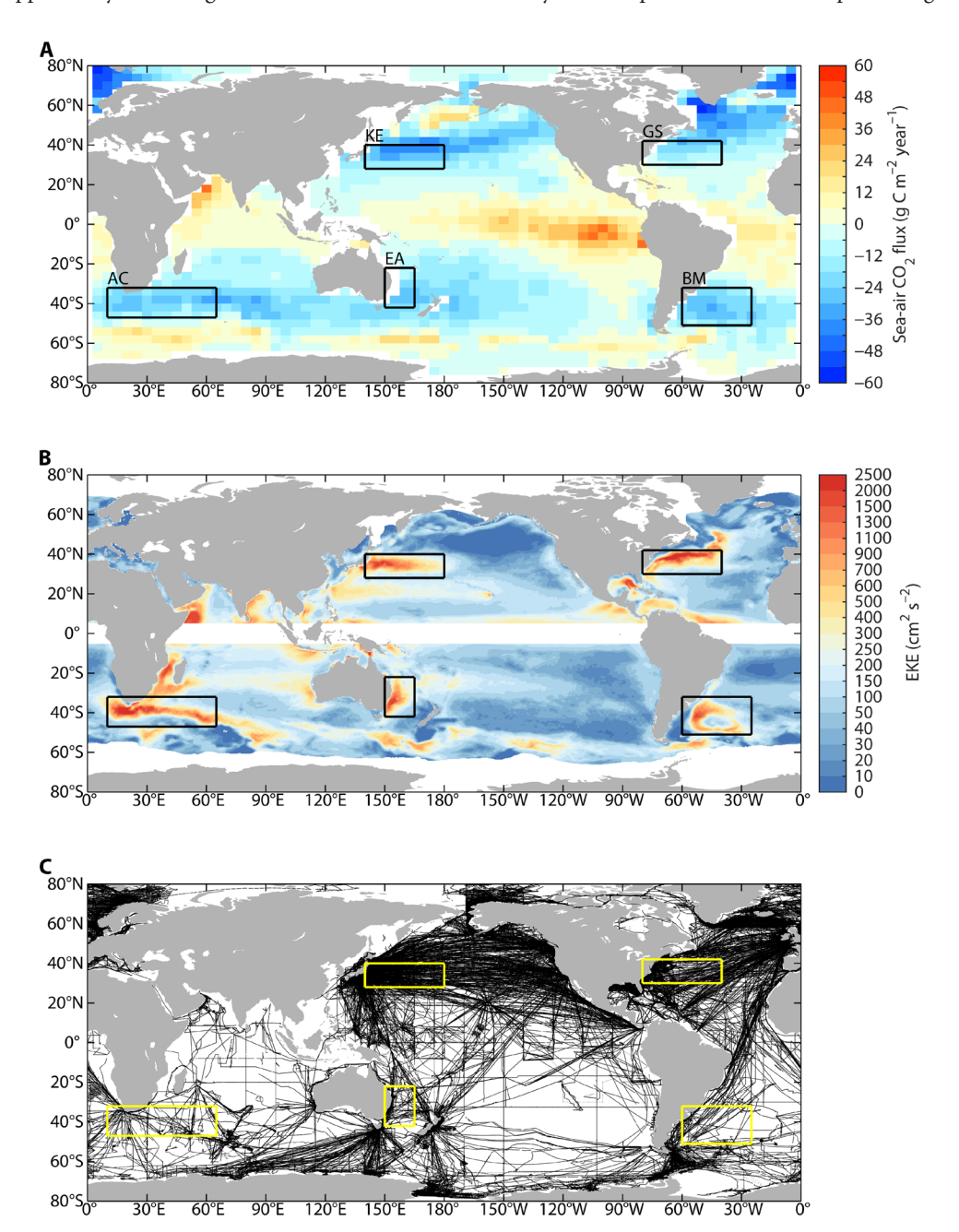


Fig. 1. WBC confluence regions featured by abundant mesoscale eddies and substantial CO₂ absorption. (A) Climatological-mean annual sea-air FCO₂ (g C m⁻² year⁻¹) for the reference year 2000 derived from Takahashi *et al.* (2). Negative values denote oceanic absorption of CO₂, while positive values denote oceanic outgassing. (B) Climatological-mean EKE (cm² s⁻²) during 1993 to 2021. (C) Distribution of surface seawater pCO₂ observations in SOCATv2022 over 1993 to 2021. Black dots mark the sample locations from each cruise. The KE region (28°N to 40°N, 140°E to 180°E), the GS region (30°N to 42°N, 80°W to 40°W), and the other three WBC confluence regions are delineated by a box. Note that the KE region has the most extensive in situ observations among the WBC regions, while data availability in Southern Hemispheric WBC regions is extremely limited.

absorption induced by anticyclonic eddies and a lower decrease by cyclonic eddies. The same methodology is applied to the Gulf Stream (GS) region, albeit with fewer available observations (fig. S1B), yielding consistent findings. The presence of active eddies likely enhances the overall $\rm CO_2$ sink in the KE region and GS region by ~10 and 14%, respectively, compared to typical estimations of FCO₂ that do not resolve these mesoscale features.

RESULTS

Net enhanced uptake of atmospheric CO₂

To assess the modification of mesoscale eddies on sea-air FCO₂, we first identify 596 anticyclonic eddies and 730 cyclonic eddies based on the criteria ensuring their intrinsic nature within the KE region and adequate temporal coverage of observations (see the "Mesoscale eddy identification" section). On average, the anticyclonic and cyclonic eddies have radii of 77.90 and 70.66 km within their lifespan, with respective lifetimes of 159 and 155 days, accompanied by amplitudes measuring 14.01 and 15.87 cm (fig. S2). Spatially, anticyclonic eddies frequently occur to the north of the KE, while cyclonic eddies are mainly located to the south (fig. S3). These distinct spatial distributions align with previous findings (34, 35), indicating a directional pattern of eddy shedding from the KE inertial jet.

We then use a feed-forward neural network (FNN; fig. S4A) to estimate eddy-associated seawater pCO₂ and derive corresponding sea-air FCO₂, isolating eddy effects on FCO₂ relative to backgrounds (see the "Eddy-associated sea surface pCO₂ reconstruction by FNN" section). Our anomaly-focused approach facilitates the effective isolation of mesoscale signals from large-scale backgrounds, enabling the precise quantification of eddy effects on FCO₂ without reliance on a predefined mesoscale spatial scale. The FNN-predicted pCO₂ shows a high level of agreement with the observed pCO₂ from Surface Ocean CO₂ Atlas (SOCAT) across training, validation, and independent test datasets, confirming robust generalization to unsampled conditions (fig. S4, B and C). Notably, the FNN-derived FCO₂ accurately reproduces a prominent seasonal cycle as observed (2, 36): CO₂ absorption markedly increases during winter, while it approaches neutrality during summer (fig. S4D). The precise portrayal of this seasonal variation substantiates the reliability of our machine learning-based approach.

The potential of eddies to modify sea-air FCO₂ is assessed through an area-weighted average FCO₂ for each eddy, where the summation is performed over the entire lifespan of the eddy (see the "Sea-air FCO₂ estimation" section). This estimation ensures the lifetimeintegrated effect of each eddy on FCO2, with varying areas throughout its life cycle taken into account. In general, both anticyclonic and cyclonic eddies in the KE region act as CO₂ sinks (Fig. 2A). On average, an anticyclonic eddy exhibits a stronger CO2 sink with a mean FCO_2 of -33.77 ± 1.90 g C m⁻² year⁻¹, which is ~40% higher than the cyclonic eddy-induced mean FCO₂ of -23.47 ± 1.25 g C m⁻² year⁻¹. Note that these absolute FCO₂ estimates encompass fluxes from both mesoscale and large-scale environmental drivers. For instance, the higher prevalence of cyclonic eddies south of the KE (fig. S3), where large-scale winter CO₂ absorption is partially offset by summer outgassing (2, 36), contributes to a relatively lower absolute FCO₂ compared to anticyclonic eddies (Fig. 2A). To isolate the specific impact of eddies on oceanic CO₂ uptake, we assess the eddy-induced FCO₂ change by comparing the FCO₂ within the eddy's core to its surrounding background environment (see the "Eddy-induced anomalies"

section). We ensure consistency in the areas of the eddy and its background and the same temporal coverage, enabling unbiased comparisons. The result shows that anticyclonic eddies increase CO₂ absorption by 15.16% relative to the background, whereas cyclonic eddies reduce it by 5.67% (Fig. 2B). The findings also hold for the GS region, where there are fewer observations of seawater pCO₂, based on the same methodology: Anticyclonic eddies induce an 18.48% increase in CO₂ absorption, which is partially counterbalanced by a 5.04% reduction because of cyclonic eddies (fig. S5). Therefore, despite the comparable properties in terms of lifespans, radii, and amplitudes between anticyclonic and cyclonic eddies, they can ultimately lead to an overall enhancement in oceanic CO₂ uptake.

By using the mean value of eddy-associated FCO₂ and its mean percentage change relative to the background, we can evaluate the additional FCO₂ into the eddy (Table 1). There is an additional FCO₂ of 4.45 ± 0.57 g C m⁻² year⁻¹ being absorbed into anticyclonic eddies, while cyclonic eddies reduce absorption by $1.41 \pm 0.39 \,\mathrm{g \, C \, m^{-2} \, year^{-1}}$ in the KE region. Similar results apply to the GS region, where anticyclonic eddies enhance CO_2 uptake by 3.45 ± 1.69 g C m⁻² year⁻¹, while cyclonic eddies reduce it by $1.01 \pm 0.46 \text{ g C m}^{-2} \text{ year}^{-1}$. The summation of these additional eddy-induced FCO2 is further compared with a representative estimate of sea-air FCO₂ based on Sea-Flux (37), which incorporates six widely used datasets of sea surface pCO₂ at monthly 1° grids, with mesoscale signals largely smoothed out (fig. S6). Quantitatively, mesoscale eddies overall contribute to enhanced uptake values of CO_2 by 9.98 ± 2.28 and $13.82 \pm 9.94\%$ in the KE and GS regions, respectively. We further use areas of 5.35 and 4.95 million km² for the KE and GS regions to estimate equivalent carbon sink (Tg C year⁻¹), which matters to the global carbon budget (4). Despite comprising only 1.48 and 1.37% of the global ocean area (362.41 million km²), these regions contribute ~8 and 4% of the global ocean carbon sink (1958.80 Tg C year⁻¹), respectively. Concurrently, anticyclonic eddies enhance carbon sink by -23.81 ± 3.05 (-17.08 ± 8.37) Tg C year⁻¹, while cyclonic eddies reduce it by $7.54 \pm 2.09 \ (5.00 \pm 2.28) \ {\rm Tg \ C \ year}^{-1}$ in the KE (GS) region. On average, mesoscale eddies contribute an additional -28.34 ± 9.41 Tg C year⁻¹ (sum of 16.26 \pm 3.69 and 12.08 \pm 8.66; Table 1) to the carbon sink across both regions. This represents an unnoticed ecosystem service, with an estimated value exceeding €50 billion annually when valued at a typical marginal abatement cost of €200 per ton of CO₂ compatible with a 1.5°C target (38).

Mechanism for the enhanced uptake

Previous case studies suggest that mesoscale eddies have the potential to modulate sea-air FCO₂ primarily through solubility (thermal)driven or nonthermal (dynamically/biologically)-driven ways. The former involves the eddy-driven changes in sea surface temperature (SST) and sea surface salinity (SSS), which alter CO_2 solubility (29). The latter involves the eddy-induced anomalies in the total concentration of DIC (22-27). There are four well-recognized processes by which eddies can cause changes in substance concentrations (e.g., chlorophyll and DIC): eddy stirring, eddy trapping, eddy pumping, and eddy-wind interaction (also referred to as eddy-induced Ekman pumping) (30, 31). Eddy stirring enhances horizontal mixing, particularly in the presence of a directional gradient in background variables (39, 40). Nonlinear eddies can confine fluids and maintain their properties within their interiors for prolonged periods through eddy trapping (41, 42). Vertical displacement of isopycnals associated with eddy pumping is generally opposite to those caused by eddy-wind

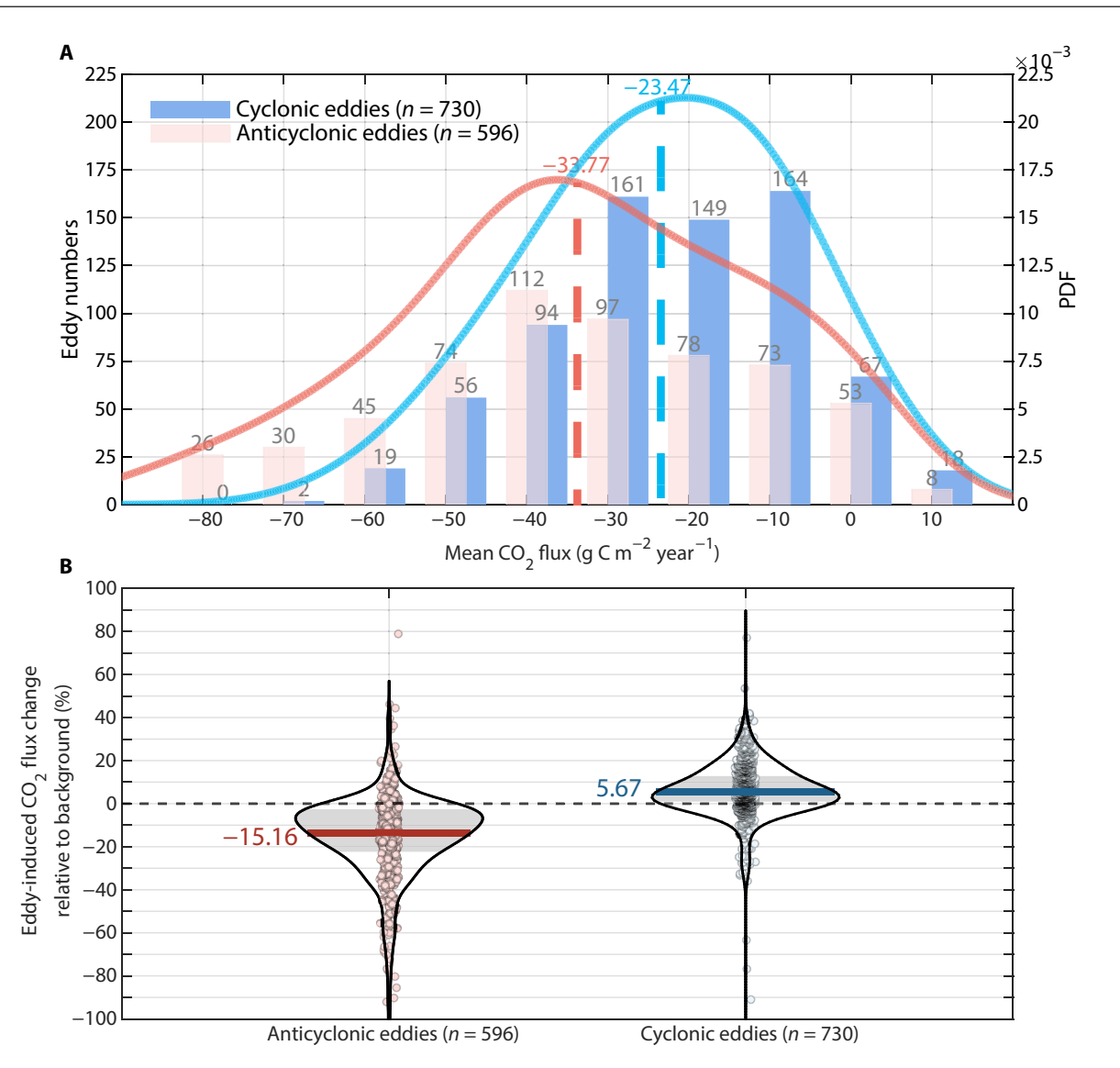


Fig. 2. Enhanced CO₂ uptake by anticyclonic eddies outweighing the reduction caused by cyclonic eddies. (A) Histogram of area-weighted average FCO₂ over the lifetimes of 596 anticyclonic eddies (red bars) and 730 cyclonic eddies (blue bars) in the KE region. The solid red and blue lines represent the probability density function (PDF) for anticyclonic and cyclonic eddies, respectively. The dashed lines indicating the mean FCO₂ are also presented. (B) Percentage change in eddy-induced FCO₂ relative to the background conditions, shown for 596 anticyclonic eddies (red dots) and 730 cyclonic eddies (blue dots). Each dot represents the result of an individual eddy. A positive value signifies a reduction in oceanic CO₂ uptake, while a negative value signifies an increase in uptake. The black envelopes illustrate the PDF. Shading areas outline the interquartile ranges. The value alongside the red/blue line denotes the mean percentage change for anticyclonic/cyclonic eddies.

interaction, resulting in contrasting anomalies of tracers within eddies relative to the background environment (43-45). For instance, eddy pumping in anticyclonic eddies typically causes negative chlorophyll anomalies, whereas eddy-induced Ekman pumping produces near-surface positive anomalies via upward transport because of eddy-induced Ekman divergence (31). The opposite occurs in cyclonic eddies. However, the dominant controlling mechanisms remain inadequately understood, and further investigation is warranted.

The mechanisms by which eddies influence sea-air FCO₂ can be inferred from the correlations between eddy-induced anomalies in FCO₂ and physical and biological variables (Fig. 3, A to C). Initially, the observed negative correlation between SST and FCO₂ anomalies (Fig. 3A) likely reflects processes beyond solubility effects, as higher

SST typically hinders CO₂ uptake (29). Elevated chlorophyll a (Chl a) concentrations, indicative of enhanced biological activity, coincide with reduced CO₂ uptake (Fig. 3B), suggesting that biological CO₂ drawdown is outweighed by other processes. Furthermore, a significant negative correlation links deeper mixed layer depth (MLD) with enhanced CO₂ uptake (Fig. 3C), which cannot be captured in our FNN framework because of the exclusion of MLD as an input parameter. In light of the aforementioned correlations, it can be reasonably inferred that the vertical movements of isopycnals, associated with eddy pumping in anticyclonic (downward) and cyclonic (upward) eddies, are likely to constitute a primary contributing factor. Eddy pumping exerts a direct influence on both chlorophyll (46, 47) and DIC (25), which in turn affect sea surface pCO₂. For instance,

Table 1. Contribution of mesoscale eddies to oceanic CO₂ uptake. Values are presented as the means \pm uncertainties, and values without/with parentheses represent the KE/GS region. The mean FCO₂ (term A, first row) encompass fluxes from both mesoscale and large-scale environmental drivers. The mean percentage change in FCO₂ because of eddies (term B, second row) allows for the estimation of large-scale background FCO₂ as Term A/(1 – Term B). Then, the additional FCO₂ into eddy (term C, third row) is derived as Term A – Term A/(1 – Term B). The FCO₂ in the KE (GS) region without eddies (term D) is estimated from SeaFlux, and the additional change by eddies (term E) is calculated by summing term C of anticyclonic and cyclonic eddies. The net effect of eddies on oceanic CO₂ uptake in the KE (GS) region (term F) is expressed as a percentage change by dividing term E by term D. The equivalent carbon sink is estimated on the basis of an area of 5.35 (4.95) million km² for the KE (GS) regions.

	Anticyclonic eddies	Cyclonic eddies	
$Mean FCO_2 (g C m^{-2} year^{-1}) (A)$	$-33.77 \pm 1.90 (-22.09 \pm 2.06)$	$-23.47 \pm 1.25 (-19.10 \pm 1.27)$	
Mean percentage change in FCO ₂ relative to background (%) (B)	-15.16 ± 1.73 (-18.48 ± 8.89)	5.67 ± 1.54 (5.04 ± 2.28)	
Additional FCO ₂ into eddy (g C m $^{-2}$ year $^{-1}$) (C)	-4.45 ± 0.57 (-3.45 ± 1.69)	1.41 ± 0.39 (1.01 ± 0.46)	
	Estimations without eddies (D)	Additional change by eddies (E)	Percentage change (F)
FCO ₂ in the KE (GS) region (g C m ⁻² year ⁻¹)	$-30.46 \pm 0.76 (-17.65 \pm 0.92)$	-3.04 ± 0.69 (-2.44 ± 1.75)	9.98 ± 2.28% (13.82 ± 9.94%)
Equivalent carbon sink in the KE (GS) region (Tg C year ⁻¹)	-162.96 ± 4.07 (-87.37 ± 4.55)	-16.26 ± 3.69 (-12.08 ± 8.66)	-

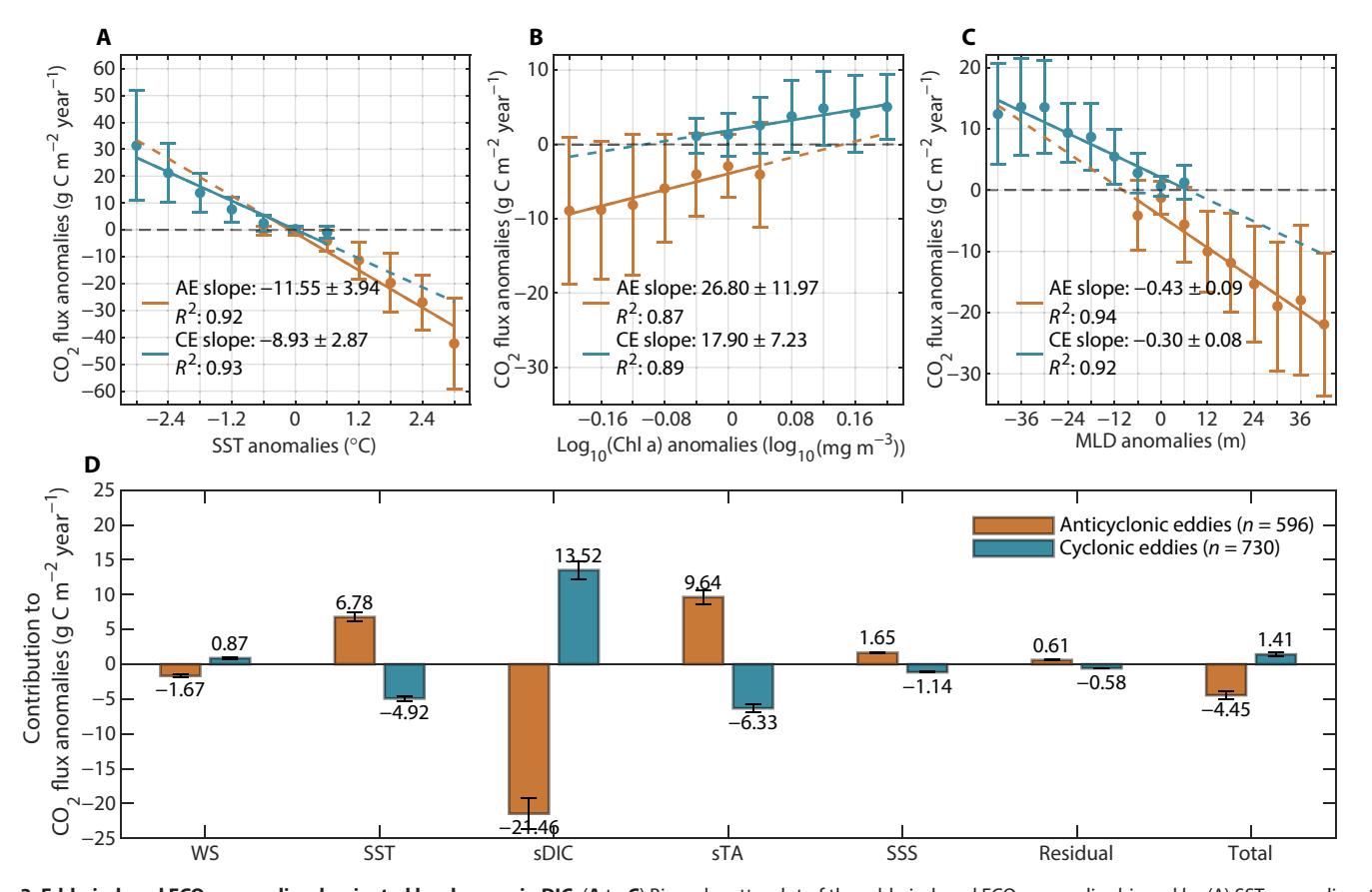


Fig. 3. Eddy-induced FCO₂ anomalies dominated by changes in DIC. (A to C) Binned scatterplot of the eddy-induced FCO₂ anomalies binned by (A) SST anomalies at every 0.6°C bin, (B) base-10 logarithm of ChI a anomalies at every 0.04 $\log_{10}(mg \, m^{-3})$ bin, and (C) ocean MLD anomalies at every 6-m bin for anticyclonic eddies (orange) and cyclonic eddies (blue) in the KE region. Points and error bars denote the mean value and the standard deviation of each bin, respectively. The line represents the linear regression with statistics showing the slope \pm 95% confidence interval and coefficient of determination (R^2). Dashed lines extend regression beyond data ranges for consistent plotting. (D) Taylor decomposition of the eddy-induced FCO₂ anomalies into contributions from the eddy-driven changes in surface wind speed (WS), SST, sDIC, salinity-normalized total alkalinity (sTA), and SSS. Any other unaccounted effects are included in the residual term. Error bars represent the 95% confidence interval for each component.

in situ case studies have demonstrated the crucial role of vertical DIC transport in increasing sea surface pCO_2 within a cold-core cyclonic eddy in the subtropical North Pacific gyre (25) and the northern Philippine Sea (48).

To quantitatively assess the effect of DIC transport, we decompose the eddy-induced FCO₂ anomalies into physical and biogeochemical components associated with mesoscale eddies (see the "Taylor decomposition of eddy-induced FCO2" section). Among these components, the primary determinant is salinity-normalized DIC (sDIC) anomalies, which reflect changes in DIC independent of salinity variations (Fig. 3D). Within anticyclonic eddies, the downward displacement of isopycnals potentially reduces the nutrient availability and associated biological activity, thus limiting biological consumption of CO₂. However, the concurring relative DIC deficit in the upper water column because of the downwelled water exerts a predominant impact by augmenting the uptake of CO₂. Conversely, within cyclonic eddies, increased biological activity is outpaced by DIC-rich waters uplifted from deeper layers, ultimately leading to the positive relationship between reduced CO₂ uptake and elevated Chl a levels (Fig. 3B). The displacement of isopycnals is evident in MLD, with a downward shift typically corresponding to an increased MLD (49). Although deeper mixed layers may facilitate nutrient mixing and subsequent primary production, severe light limitation in the midlatitude oceans, particularly during winter when eddy-induced MLD deepening is most pronounced, can overpower these benefits (19, 30, 49, 50). Therefore, the deepening mixed layers observed within anticyclonic eddies, associated with downward eddy pumping, reduce DIC levels and consequently facilitate increased CO2 uptake despite suppressed primary production in surface waters (Fig. 3C).

The other three processes (eddy-wind interaction, eddy stirring, and eddy trapping) that influence surface DIC concentrations are also taken in consideration and discussed. The dominance of eddywind interaction is not possible, given its tendency to produce conflicting anomalies compared to the observed ones (Fig. 3, A to C). Nevertheless, it may counteract, to some extent, the eddy pumping effects. Although eddy stirring often results in dipole-type anomalies (51, 52), their overall impact is likely minimal because of general cancellation of these anomalies when averaged over the radius of an eddy (53). Eddy trapping may be operative, particularly under background conditions characterized by a meridional distribution, as observed in the KE region regarding DIC and Chl a concentrations (fig. S7, A and B). Here, an approximately equal number of anticyclonic eddies are observed to move both northward and southward, indicating that the potential impact of eddy trapping could be mitigated in general and have a minor overall effect (fig. S7, A and C). In contrast, a greater proportion of cyclonic eddies exhibits southward movement, hypothetically trapping DIC- and chlorophyll-rich seawaters from the northern to southern areas (fig. S7, B and C). The temporal evolutions of DIC and Chl a anomalies induced by eddies throughout their lifetimes, however, show that the mean changes in DIC and Chl a anomalies for eddies moving southward are almost equal to those moving northward, irrespective of their types (fig. S8, solid lines). This observation contradicts the hypothesis that more pronounced anomalies would be associated with cyclonic eddies moving southward if eddy trapping effects were dominant (fig. S8, dashed lines). Ultimately, we identify eddy pumping as the primary governing process for the overall mesoscale modulations of FCO₂.

Although eddy pumping of DIC generally plays a dominant role in governing modifications of both anticyclonic and cyclonic eddies on FCO₂, it is expected to be partially hindered within cyclonic eddies because of nutrient supply for biological production and associated biological CO₂ consumption, resulting in overall asymmetric changes in FCO₂ within anticyclonic and cyclonic eddies. Further inspection evidences that the reduction in sDIC given per unit increase in MLD within anticyclonic eddies is approximately equivalent to the opposite changes within cyclonic eddies (exhibiting nearly identical linear slopes; fig. S9A). However, the responses of Chl a to a unit change in MLD are asymmetric: A substantial increase in Chl a is observed within cyclonic eddies, while anticyclonic eddies exhibit a more moderate decrease, as evidenced by the steeper negative slope for cyclonic eddies (fig. S9B). It is suggested that the decrease in biological activity within anticyclonic eddies is likely constrained by the background level because of the prevailing oligotrophic restriction, while the increase in biological production within cyclonic eddies can be relatively more pronounced because of the high sensitivity of phytoplankton groups to nutrient supply (54, 55). Thus, the alteration of biological activity is likely to have greater consequences in cyclonic eddies compared to anticyclonic eddies, such as a substantial compensatory effect through enhanced biological CO₂ consumption.

DISCUSSION

Our finding of the net enhancement in oceanic CO_2 uptake by mesoscale eddies is underpinned by the observation-based estimations of eddy-induced sea-air FCO_2 anomalies obtained through tracking thousands of eddies and reconstructing eddy-associated sea surface pCO_2 using our FNN model. The downward pumping of DIC within anticyclonic eddies primarily governs the enhanced uptake (Fig. 4). We quantify that mesoscale eddies contribute to additional CO_2 uptake values of ~10 and 14% in the KE and GS regions, which are recognized as two major areas for ocean carbon sinks in the Northern Hemisphere.

Previous observational studies examining individual eddies have reported contrasting results regarding their influence on sea-air FCO₂. Some studies, consistent with our findings, documented enhanced oceanic CO₂ uptake by warm-core anticyclonic eddies (22, 26) and reduced uptake by cold-core cyclonic eddies (25, 28), attributing these effects primarily to the dominant role of eddy pumping. Conversely, opposite outcomes have also been observed, such as reduced CO₂ uptake by warm-core anticyclonic eddies (27). These discrepancies could arise from methodological limitations, including insufficient eddy sampling, regional variability, and differences in eddy characteristics such as their stage within the eddy lifespan (23, 24). The contrasting effects of individual eddies are illustrated in Fig. 2B, aligning with the differences reported in previous case studies. Eddy-induced seaair FCO2 anomalies exhibit distinct evolutions across different eddy lifespan stages (fig. S10). Anticyclonic eddies drive enhanced oceanic CO₂ uptake during the growth stage as intensifying eddy pumping dominates, while counteracting processes exert increasing influence during the maturity stage and become more prominent during the decay stage. For cyclonic eddies, while eddy pumping initially drives a reduction in CO₂ uptake, its effectiveness appears to diminish rapidly, likely due to the counteracting influence of intensified biological processes. This highlights the complex evolution of eddy-induced FCO₂ anomalies throughout the eddy lifetime, necessitating further detailed analysis. Nevertheless, our results underscore the importance of analyzing a large ensemble of eddies over their full lifespans to derive statistically robust estimates of their net impact on sea-air

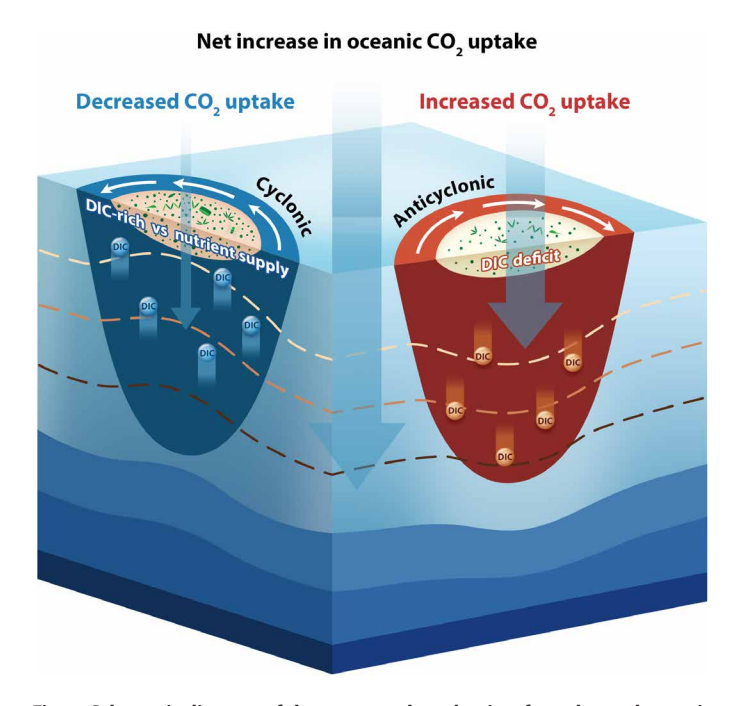


Fig. 4. Schematic diagram of the suggested mechanism for enhanced oceanic CO_2 uptake by mesoscale eddies. Anticyclonic and cyclonic eddies, rotating clockwise and counterclockwise in the Northern Hemisphere, are represented in red and blue, respectively. Anticyclonic eddies are characterized by the downward displacement of isopycnals (depicted as blue layers), which pumps the surface low-DIC water into deeper layers (illustrated as the downward shift of stratified boundaries of DIC in brown). The relative DIC deficit in surface water leads to a decrease in sea surface p CO_2 , thereby enhancing CO_2 uptake despite nutrient restriction. Conversely, the elevated levels of DIC in surface waters because of the upwelled import within cyclonic eddies weaken CO_2 uptake. This effect, however, could be partially counterbalanced by enhanced biological CO_2 absorption because of concurrent nutrient supply from deeper waters. As a result, the reduction in CO_2 uptake within cyclonic eddies is less pronounced compared to that enhanced by anticyclonic eddies, leading to an overall increase in oceanic CO_2 sink.

FCO₂. Beyond the climatological-mean eddy effects elucidated by this approach, it would be valuable to analyze the contributions of eddy-induced FCO₂ anomalies to seasonal variations and long-term trends in ocean carbon sink in future studies.

Our results indicate that the current estimation of the ocean's capacity to sequester CO₂, which is based on limited observations and eddy-parameterizing models without fully considering ocean mesoscales in CO₂ dynamics (4), is likely underestimated. Given the dearth of observations, it is currently unfeasible to ascertain an exact figure for this underestimation. It is therefore crucial to consistently invest in observational efforts in marine carbonate systems, particularly in the severely underrepresented southern oceans enriched with eddies, aiming to accurately assess the oceanic capability for CO2 storage while taking into account the eddies' effects (56). Nevertheless, using the eddy-induced additional FCO₂ change rate relative to the background offers an advantage of extrapolating the average percentage change rate in the KE and GS regions (11.90 \pm 5.10%; Table 1) to analogous areas. For instance, this insight could be applicable to other midlatitude oceans in both hemispheres characterized by pronounced seasonal variations in light and nutrient availability, as well as light limitations for phytoplankton during winter (19), particularly those WBC regions with strong carbon sinks (Fig. 1A). If this

change rate is ideally generalized to the global ocean, a hypothetical underestimation (additional CO₂ storage by mesoscale eddies) would be 233.10 \pm 100.33 Tg C year $^{-1}$ in the context of a global average carbon sink of 1958.80 \pm 78.19 Tg C year $^{-1}$ (estimated from SeaFlux) that is primarily contributed by the midlatitude oceans. This additional CO₂ storage amounts to ~59.7 \pm 25.7% of the uncertainty in oceanic CO₂ uptake (390.5 Tg C year $^{-1}$) during 2013 to 2022 (4) or ~25% of the global CO₂ emitted by fossil fuel combustion from cars and vans in 2022 (963.4 Tg C) (57). This suggests a possible global impact of eddies on the ocean carbon sink, yet future studies are warranted to determine the precise outcome.

Considering the increase in upper ocean eddy activity observed in the satellite altimetry record (58) and projected under the global warming scenario (59), it is expected that the influence of ocean eddies on carbon uptake becomes increasingly substantial in the future. The eddy-resolving simulations have suggested that more than 30% of sea-air FCO₂ variability is linked to oceanic mesoscale flows in eddy-rich regions (32), and a stronger oceanic CO₂ sink is anticipated in a warming climate compared to the simulation at a 1° coarse resolution (60). As such, incorporating a realistic portrayal of ocean eddies in Earth System models is of paramount importance for a comprehensive evaluation of current and future states of the oceans and global climate.

MATERIALS AND METHODS

Satellite datasets

We use daily and monthly mean 4-km resolution Chl a composites from the Ocean Colour Climate Change Initiative (OC-CCI) version 5 (61). The OC-CCI product integrates ocean color data from multiple satellite sensors, including the Moderate Resolution Imaging Spectroradiometer on Aqua (MODIS-A), Medium Resolution Imaging Spectrometer, Sea-viewing Wide Field-of-view Sensor, and Visible Infrared Imaging Radiometer Suite. This composite product is bias corrected and quality controlled, substantially reducing data gaps compared to data from individual sensors. Coincident 4-km resolution daily and monthly mean composites of SST and photosynthetically active radiation (PAR) are obtained from MODIS-A (62, 63). To ensure adequate data coverage, Chl-a, SST, and PAR data are subjected to a 7-day running mean. These variables are used to estimate daily and monthly net primary production (NPP) by using the Wavelength Resolving Model (64). Our analysis covers the period from July 2002 to December 2021, during which all observations required are available.

The Global Ocean Gridded L4 Sea Surface Heights and Derived Variables Reprocessed 1993 Ongoing product (65) provided by the Copernicus Marine Environment Monitoring Service (CMEMS) are used to estimate oceanic eddy kinetic energy (EKE). EKE calculations are based on deviations from the 270-day running mean of zonal and meridional geostrophic velocity anomalies (66), with exclusion near the equator where geostrophic balance is not maintained.

Reanalysis datasets

Daily and monthly mean SSS data are taken from a global eddy-resolving physical ocean and sea ice reanalysis (GLORYS12) (67) provided by CMEMS, with a quasi-isotropic horizontal grid spacing of 1/12° (~8 km) and 50 vertical levels (resolution starting at 1 m near the surface and extending to 450 m at depths of 5000 m). The data assimilation used a reduced-order Kalman filter, incorporating

various observations such as satellite-derived AVHRR SST and in situ vertical profiles of temperature and salinity from the CMEMS CORA quality-controlled database. In addition, daily MLD is also sourced from GLORYS12. The MLD within this dataset is defined as the depth where the density exceeds the reference density (at 10 m) by an amount equivalent to a 0.2°C temperature decrease under local surface conditions. Furthermore, daily surface (10 m) wind speed data at a resolution of 0.25° are acquired from the Cross-Calibrated Multi-Platform (CCMP) version 3.1 product, which integrates ocean surface wind retrievals from various satellite microwave sensors and supplements these with a background field derived from ERA5 10-m neutral stability winds.

Observational datasets

SOCAT version 2022 cruise track dataset compiles global observations dating back to 1970, which have undergone extensive automatic and manual secondary quality controls (68). Here, in situ data from 2002 to 2021 pertinent to the KE and GS regions are extracted. Observations typically originated from depths beyond the mass boundary layer where gas exchange occurs (69, 70). Therefore, we adjust SOCAT data to a standard temperature level and depth corresponding to the base of the mass boundary layer using daily 0.25° NOAA Optimum Interpolation SST (OISST) version 2 (71). The adjusted fugacity of CO_2 in seawater is converted to pCO_2 and binned into 0.25° monthly grids in accordance with SOCAT protocols (72). Uncertainties in the reanalyzed observation data are considered as the standard deviation within each grid cell or set at 5 µatm where only a single observation existed (73). The processing steps, following Goddijn-Murphy et al. (74), are implemented using the open-source FluxEngine toolbox (75, 76).

For comparison, we use SeaFlux that uses a consistent approach specifically targeting the most commonly used pCO₂ data products to deliver an end-product for intercomparisons within assessment studies (37). It is based on six observation-based pCO₂ products covering 1990 to 2019, including three neural network-derived products (CMEMS-FFNN, MPI-SOMFFN, and NIES-FNN), a mixed layer scheme product (JENA-MLS), a multiple linear regression (JMA-MLR), and a machine learning ensemble (CSIR-ML6). By using a uniform methodology in FCO₂ calculation, the difference in the resulting flux estimates can be attributed to the mapping method and wind products used. By filling the missing areas, especially the coastal regions, SeaFlux provides the global coverage of sea surface pCO₂ and sea-air FCO₂ at monthly 1° grids. Here, the average of the FCO₂ estimates derived from the six products is used.

Mesoscale eddy identification

On the basis of the Mesoscale Eddy Trajectory Atlas Product (META version 3.2) all-satellites version provided by AVISO, we tracked the daily latitude, longitude, amplitude, and radius of eddy that satisfies the following criteria: (i) The eddy originates within the target region; (ii) the eddy dissipates within the target region; (iii) the eddy lifespan starts after 4 July 2002 and ends before 1 January 2022; (iv) the eddy lives at least 12 weeks. The first two criteria ensure that eddies are intrinsic localized perturbations, allowing for accurate estimation of pCO₂ in seawater using our FNN without requiring extrapolation. The third criterion addresses the availability of observational data. The fourth criterion balances the need for a sufficient observational time frame against maintaining an adequate sample number of eddies under the consideration of previously used eddy durations

ranging from 4 weeks (34) to 16 weeks (13). In addition, eddies with missing monthly mean Chl a values throughout their lifespan are excluded because of data gaps in Chl a, forming the fifth implicit requirement. The influence of each requirement on eddy selection is shown in table S1, with the threshold of eddy lifespan having the greatest impact. Nevertheless, 596 anticyclonic eddies and 730 cyclonic eddies are identified in the KE region, constituting a large ensemble. On the basis of the same criteria, we also identified 527 anticyclonic eddies and 726 cyclonic eddies in the GS region.

Eddy-induced anomalies

We extract the daily mean data from a circular area extending to one radius from the eddy center, provided that at least 10% of the data within this area are available. This designated area represents the eddy's core, where substantial impacts from the eddy are anticipated. Meanwhile, a ring-shaped area extending from one to three times the eddy's radius serves as the background zone. Monthly means of daily values for both areas are then calculated. The eddy-induced anomalies are defined as the difference in values between the eddy's core and its background.

Eddy-associated sea surface pCO₂ reconstruction by FNN

To address the observational limitations of sea surface pCO₂, machine learning approaches, particularly those involving FNN, have been used. These approaches use various combinations of predictors to successfully reconstruct the global distribution and interannual variability of sea surface pCO₂ (4, 69, 77–82). Previous study underscores the crucial influence of the distribution of surface ocean pCO₂ observations on the efficacy of FNN models (77). The KE region occupies a larger number of observations compared to other regions (Fig. 1C and fig. S1), resulting in more reliable reconstructions.

Following established methodologies, we selected a set of predictors for our FNN: atmospheric pCO₂, NPP, SST, SSS, latitude (LAT), longitude (LON), cosine of month (CMON), sine of month (SMON), and the number of months since July 2002 (nMON). These predictors combine physical, biological, and spatiotemporal elements

$$pCO_{2,sea} =$$

FNN [pCO_{2.air}, log₁₀(NPP), SST, SSS, LAT, LON, CMON, SMON, nMON]

$$CMON = \cos\left(Month \times \frac{\pi}{6}\right) \tag{2}$$

$$SMON = \sin\left(Month \times \frac{\pi}{6}\right)$$
 (3)

To facilitate training, all monthly predictors are remapped to a uniform 0.25° grid spacing (fig. S1). Considering the biological consistency within the KE/GS region (50, 83), there is no necessity for further subdivision into more intricate biological provinces. Moreover, our FNN framework benefits from incorporating spatiotemporal predictors, rendering such a subdivision unnecessary (81).

During pretraining, the number of neurons was incrementally adjusted from 2 to 100, with increments of two neurons up to 50 and 10 thereafter. The SOCAT pCO₂ (see the "Observational datasets" section for 0.25° postprocessing) and all predictor datasets were divided into two subsets using the optimal split method (84): a training dataset (75%) to train the FNN and a validation dataset (25%) to evaluate performance and prevent overfitting (fig. S11). To ensure sample independence and avoid overfitting, a group K-fold cross-validation was applied, splitting data by year (80, 82): For every four consecutive years, three were used for training and one for validation, iterated four times to compute the average root mean square error. The neuron count yielding the lowest root mean square error was selected for final training. For final training, 10% of the data were reserved as an independent test set, while the remaining data underwent 10 randomized splits into training (70%) and validation (20%) sets, producing an ensemble of 10 FNN models (77). Their averaged outputs formed the final prediction (77). The trained FNN then estimated sea surface pCO₂ for eddy's core and its background by using the monthly mean of daily predictor values from corresponding regions (see the "Eddy-induced anomalies" section for definitions of the eddy's core and its background). Note that our FNN-based reconstruction is tailored for reconstructing eddy-associated sea surface pCO₂, which effectively isolates mesoscale signals from large-scale backgrounds.

Sea-air FCO₂ estimation

The sea-air FCO2 is calculated using a bulk formula

$$FCO_2 = k \left(\alpha_{\text{sea}} pCO_{2,\text{sea}} - \alpha_{\text{air}} pCO_{2,\text{air}} \right)$$
 (4)

where the gas transfer velocity $k=0.251 U_{10}^2 \left(\frac{Sc}{660}\right)^{-0.5}$ is estimated from surface wind speed (U_{10}) and Schmidt number (Sc) (85); the solubility of CO2, represented by α_{sea} and α_{air} at the base and top of the mass boundary layer, respectively (70), is calculated as a function of the temperature and salinity (29). For these calculations, subskin SST and SSS are used for α_{sea} , while skin SST and SSS are used for α_{air} , incorporating a cool skin effect of 0.17 K (86) to covert skin SST to subskin SST and a salinity increase of 0.1 unit (70, 87) to convert subskin SSS to skin SSS. The average daily FCO₂ of both the eddy' core and its background are calculated for each month along the eddy trajectory by using the FNN-predicted sea surface pCO₂ (pCO_{2.sea}). Atmospheric pCO₂ (pCO_{2.air}) is estimated for the average location of the eddy throughout the month without distinguishing between the eddy's core and its background.

The area-weighted average FCO₂ for each eddy's core and its

background is calculated as
$$\frac{\displaystyle\sum_{i=1}^{\text{Last month}} \text{FCO}_2^i \times \pi \overline{R}_i^2}{\displaystyle\sum_{i=1}^{\text{Last month}} \pi \overline{R}_i^2}, \text{ where } \overline{R} \text{ is the }$$

monthly average eddy radius, with the summation performed over

each eddy's lifespan. Then, the percentage change in area-weighted average FCO₂ between the eddy's core and its background is estimated as $\frac{FCO_2^{eddy} - FCO_2^{background}}{|FCO_2^{background}|}$. A positive value indicates a stronger source or a weaker sink for atmospheric CO2. To mitigate the influence of extreme values on the mean, we excluded the top and bottom 0.5% of the data (i.e., the remarkable outliers such as a percentage change of -2000% for anticyclonic and +1500% for cyclonic eddies), thereby retaining 99% of the data for computing

Taylor decomposition of eddy-induced FCO₂

the average.

We perform a linear Taylor decomposition of the eddy-induced FCO₂ anomalies as follows

$$\Delta FCO_2 = \frac{\partial FCO_2}{\partial WS} \Delta WS + \frac{\partial FCO_2}{\partial pCO_{2,sea}} \Delta pCO_{2,sea}$$
 (5)

where Δ signifies the eddy-induced change estimated as the difference between the eddy's core and its background, and WS is surface wind speed; $\frac{\partial FCO_2}{\partial WS}$ and $\frac{\partial FCO_2}{\partial pCO_{2,sea}}$ are derived from bulk parameterization Eq. 4 using the mean values of WS and pCO2 (88). The $\Delta pCO_{2,sea}$ values are decomposed into contributions from the eddyinduced changes in temperature (T), DIC, total alkalinity (TA), and salinity (S) (89)

$$\begin{split} & \Delta \text{pCO}_{2,\text{sea}} = \\ & \frac{\partial \text{pCO}_{2,\text{sea}}}{\partial T} \Delta T + \frac{\partial \text{pCO}_{2,\text{sea}}}{\partial \text{DIC}} \Delta \text{DIC} + \frac{\partial \text{pCO}_{2,\text{sea}}}{\partial \text{TA}} \Delta \text{TA} + \frac{\partial \text{pCO}_{2,\text{sea}}}{\partial S} \Delta S \end{split}$$

By introducing sDIC (sDIC = $\frac{S_0}{S} \times DIC$, $S_0 = 35$) and TA $(sTA = \frac{S_0}{c} \times TA)$ (88), we derive

$$\Delta pCO_{2,sea} = \frac{\partial pCO_{2,sea}}{\partial T} \Delta T + \frac{\partial pCO_{2,sea}}{\partial DIC} \frac{S}{S_0} \Delta sDIC + \frac{\partial pCO_{2,sea}}{\partial TA} \frac{S}{S_0} \Delta sTA + \left(\frac{\partial pCO_{2,sea}}{\partial DIC} \frac{sDIC}{S_0} + \frac{\partial pCO_{2,sea}}{\partial TA} \frac{sTA}{S_0} + \frac{\partial pCO_{2,sea}}{\partial S} \right) \Delta S$$
(7)

where the buffer factor γ (pCO₂ sensitivity), calculated from the mean values of TA and DIC in both the eddy's core and its background, is used to estimate the partial derivatives (90)

$$\frac{\partial \text{pCO}_{2,\text{sea}}}{\partial T} = 0.0423 \,^{\circ} \, C^{-1} \times \text{pCO}_{2,\text{sea}}$$
 (8)

$$\frac{\partial \text{pCO}_{2,\text{sea}}}{\partial \text{DIC}} = \frac{\text{pCO}_{2,\text{sea}}}{\text{DIC}} \times \gamma_{\text{DIC}}$$
 (9)

$$\frac{\partial pCO_{2,sea}}{\partial TA} = \frac{pCO_{2,sea}}{TA} \times \gamma_{TA}$$
 (10)

$$\frac{\partial pCO_{2,sea}}{\partial S} = \frac{pCO_{2,sea}}{S} \tag{11}$$

$$\gamma_{\text{DIC}} = \frac{3 \times \text{TA} \times \text{DIC} - 2 \times \text{DIC}^2}{(2 \times \text{DIC} - \text{TA}) \times (\text{TA} - \text{DIC})}$$
(12)

$$\gamma_{TA} = -\frac{TA^2}{(2 \times DIC - TA) \times (TA - DIC)}$$
 (13)

Here, TA is calculated on the basis of its relationships with SST, SSS, and longitude (91). Sea surface pCO2 and TA are then used to calculate DIC based on CO2SYS (MATLAB version 3.2.1) (92), with the carbonic acid dissociation constants from Lueker et al. (93), sulfate dissociation constants from Dickson (94), and borate-to-salinity ratio from Lee et al. (95).

On the basis of the aforementioned decompositions, we can quantify the contributions of wind speed, SST, sDIC, sTA, and SSS induced by eddies to the total FCO2 anomalies. Our focus is on assessing the relative magnitudes of those components to identify the predominant factors determining FCO₂ anomalies.

Uncertainty estimates

The uncertainty of sea surface pCO₂ predicted by the FNN is estimated by considering potential errors arising from the input parameters of the FNN, which are evaluated through Monte Carlo uncertainty propagation. In 1000 simulations, the input parameters are perturbed using random noise corresponding to their respective uncertainties. The uncertainty values for the input parameters are as follows: 0.41°C for MODIS-A SST (96), 0.22 $\log_{10}(\text{mgC m}^{-2} \text{ day}^{-1})$ for NPP (96), 1 μ atm for atmospheric pCO₂ (2), and 0.293 for SSS (97).The uncertainties in the input parameters are then combined in quadrature with the root mean square deviation of the test dataset (16.233 μ atm) to produce the combined uncertainty for sea surface pCO₂.

Next, we estimate the uncertainty of the predicted monthly average daily sea-air FCO₂ for each eddy's core and its background over its lifetime. Once again, Monte Carlo uncertainty propagation is used with 1000 simulations to propagate the uncertainties of sea surface pCO₂, atmospheric pCO₂, SST, SSS, and the gas transfer velocity k = 10%; (98)]. The standard deviation of these simulations is regarded as the monthly average daily FCO₂ uncertainty associated with methods used. Subsequently, the monthly average daily FCO₂ is used to calculate the area-weighted average FCO2 and its eddyinduced change, for which the uncertainties are also required. The method-induced uncertainties (σ_m) of the area-weighted average FCO₂ and its eddy-induced change are estimated by propagating the uncertainty of monthly average daily FCO2 using standard error propagation techniques. Last, the method-induced uncertainties are combined in quadrature with the standard error (SE) of areaweighted average FCO₂ and its eddy-induced change from all eddies to yield the final uncertainty ($\sigma = \sqrt{\sigma_m^2 + SE^2}$).

Supplementary Materials

This PDF file includes:

Figs. S1 to S11
Table S1
References

REFERENCES AND NOTES

- M. Reichstein, M. Bahn, P. Ciais, D. Frank, M. D. Mahecha, S. I. Seneviratne, J. Zscheischler, C. Beer, N. Buchmann, D. C. Frank, D. Papale, A. Rammig, P. Smith, K. Thonicke, M. Van Der Velde, S. Vicca, A. Walz, M. Wattenbach, Climate extremes and the carbon cycle. *Nature* 500, 287–295 (2013).
- T. Takahashi, S. C. Sutherland, R. Wanninkhof, C. Sweeney, R. A. Feely, D. W. Chipman, B. Hales, G. Friederich, F. Chavez, C. Sabine, A. Watson, D. C. E. Bakker, U. Schuster, N. Metzl, H. Yoshikawa-Inoue, M. Ishii, T. Midorikawa, Y. Nojiri, A. Körtzinger, T. Steinhoff, M. Hoppema, J. Olafsson, T. S. Arnarson, B. Tilbrook, T. Johannessen, A. Olsen, R. Bellerby, C. S. Wong, B. Delille, N. R. Bates, H. J. W. de Baar, Climatological mean and decadal change in surface ocean pCO₂, and net sea–air CO₂ flux over the global oceans. *Deep Sea Res. Il Top. Stud. Oceanogr.* 56, 554–577 (2009).
- P. A. Arias, N. Bellouin, E. Coppola, R. G. Jones, G. Krinner, J. Marotzke, V. Naik, M. D. Palmer, G.-K. Plattner, J. Rogelj, M. Rojas, J. Sillmann, T. Storelvmo, P. W. Thorne, B. Trewin, K. Achuta Rao, B. Adhikary, R. P. Allan, K. Armour, G. Bala, R. Barimalala, S. Berger, J. G. Canadell, C. Cassou, A. Cherchi, W. Collins, W. D. Collins, S. L. Connors, S. Corti, F. A. Cruz, F. J. Dentener, C. Dereczynski, A. Di Luca, A. Diongue-Niang, F. J. Doblas-Reyes, A. Dosio, H. Douville, F. Engelbrecht, V. Eyring, E. Fischer, P. Forster, B. Fox-Kemper, J. S. Fuglestvedt, J. C. Fyfe, N. P. Gillett, L. Goldfarb, I. Gorodetskaya, J. M. Gutiérrez, R. Hamdi, E. Hawkins, H. T. Hewitt, P. Hope, A. S. Islam, C. Jones, D. S. Kaufman, R. E. Kopp, Y. Kosaka, J. Kossin, S. Krakovska, J.-Y. Lee, J. Li, T. Mauritsen, T. K. Maycock, M. Meinshausen, S.-K. Min, P. M. S. Monteiro, T. Ngo-Duc, F. Otto, I. Pinto, A. Pirani, K. Raghavan, R. Ranasinghe, A. C. Ruane, L. Ruiz, J.-B. Sallée, B. H. Samset, S. Sathyendranath, S. I. Seneviratne, A. A. Sörensson, S. Szopa, I. Takayabu, A.-M. Treguier, B. van den Hurk, R. Vautard, K. von Schuckmann, S. Zaehle, X. Zhang, K. Zickfeld, "Techincal summary" in Climate Change 2021: The Physical Science Basis. Contribution of Working Group I to the Sixth Assessment Report of the Intergovernmental Panel on Climate Change, V. Masson-Delmotte,

- P. Zhai, A. Pirani, S. L. Connors, C. Péan, S. Berger, N. Caud, Y. Chen, L. Goldfarb, M. I. Gomis, M. Huang, K. Leitzell, E. Lonnoy, J. B. R. Matthews, T. K. Maycock, T. O. Waterfield, R. Yelekçi, B. Z. Yu, Eds. (Cambridge Univ. Press, 2021), pp. 33–144.
- 4. P. Friedlingstein, M. O'Sullivan, M. W. Jones, R. M. Andrew, D. C. E. Bakker, J. Hauck, P. Landschützer, C. Le Quéré, I. T. Luijkx, G. P. Peters, W. Peters, J. Pongratz, C. Schwingshackl, S. Sitch, J. G. Canadell, P. Ciais, R. B. Jackson, S. R. Alin, P. Anthoni, L. Barbero, N. R. Bates, M. Becker, N. Bellouin, B. Decharme, L. Bopp, I. B. M. Brasika. P. Cadule, M. A. Chamberlain, N. Chandra, T.-T.-T. Chau, F. Chevallier, L. P. Chini, M. Cronin, X. Dou, K. Enyo, W. Evans, S. Falk, R. A. Feely, L. Feng, D. J. Ford, T. Gasser, J. Ghattas, T. Gkritzalis, G. Grassi, L. Gregor, N. Gruber, Ö. Gürses, I. Harris, M. Hefner, J. Heinke, R. A. Houghton, G. C. Hurtt, Y. Iida, T. Ilyina, A. R. Jacobson, A. Jain, T. Jarníková, A. Jersild, F. Jiang, Z. Jin, F. Joos, E. Kato, R. F. Keeling, D. Kennedy, K. Klein Goldewijk, J. Knauer, J. I. Korsbakken, A. Körtzinger, X. Lan, N. Lefèvre, H. Li, J. Liu, Z. Liu, L. Ma, G. Marland, N. Mayot, P. C. McGuire, G. A. McKinley, G. Meyer, E. J. Morgan, D. R. Munro, S.-I. Nakaoka, Y. Niwa, K. M. O'Brien, A. Olsen, A. M. Omar, T. Ono, M. Paulsen, D. Pierrot, K. Pocock, B. Poulter, C. M. Powis, G. Rehder, L. Resplandy, E. Robertson, C. Rödenbeck, T. M. Rosan, J. Schwinger, R. Séférian, T. L. Smallman, S. M. Smith, R. Sospedra-Alfonso, Q. Sun, A. J. Sutton, C. Sweeney, S. Takao, P. P. Tans, H. Tian, B. Tilbrook, H. Tsujino, F. Tubiello, G. R. Van Der Werf, E. Van Ooijen, R. Wanninkhof, M. Watanabe, C. Wimart-Rousseau, D. Yang, X. Yang, W. Yuan, X. Yue, S. Zaehle, J. Zeng, B. Zheng, Global Carbon Budget 2023. Earth Syst. Sci. Data 15, 5301-5369 (2023).
- R. D. Lamboll, Z. R. J. Nicholls, C. J. Smith, J. S. Kikstra, E. Byers, J. Rogelj, Assessing the size and uncertainty of remaining carbon budgets. *Nat. Clim. Chang.* 13, 1360–1367 (2023).
- B. M. Sanderson, Estimating vanishing allowable emissions for 1.5 °C. Nat. Clim. Chang. 13, 1284–1285 (2023).
- K. Fennel, J. P. Mattern, S. C. Doney, L. Bopp, A. M. Moore, B. Wang, L. Yu, Ocean biogeochemical modelling. Nat. Rev. Methods Primers 2, 76 (2022).
- J. Hauck, M. Zeising, C. Le Quéré, N. Gruber, D. C. E. Bakker, L. Bopp, T. T. T. Chau, Ö. Gürses, T. Ilyina, P. Landschützer, A. Lenton, L. Resplandy, C. Rödenbeck, J. Schwinger, R. Séférian, Consistency and challenges in the ocean carbon sink estimate for the global carbon budget. Front. Mar. Sci. 7, 571720 (2020).
- C. A. Stock, J. P. Dunne, J. G. John, Global-scale carbon and energy flows through the marine planktonic food web: An analysis with a coupled physical–Biological model. *Prog. Oceanogr.* 120, 1–28 (2014).
- O. Aumont, C. Ethé, A. Tagliabue, L. Bopp, M. Gehlen, PISCES-v2: An ocean biogeochemical model for carbon and ecosystem studies. *Geosci. Model Dev.* 8, 2465–2513 (2015).
- X. Ruan, D. Couespel, M. Lévy, J. Li, J. Mak, Y. Wang, Combined physical and biogeochemical assessment of mesoscale eddy parameterisations in ocean models: Eddy induced advection at non-eddying resolutions. *Ocean Model.* 183, 102204 (2023).
- D. Carroll, D. Menemenlis, J. F. Adkins, K. W. Bowman, H. Brix, S. Dutkiewicz, I. Fenty, M. M. Gierach, C. Hill, O. Jahn, P. Landschützer, J. M. Lauderdale, J. Liu, M. Manizza, J. D. Naviaux, C. Rödenbeck, D. S. Schimel, T. Van der Stocken, H. Zhang, The ECCO-Darwin data-assimilative global ocean biogeochemistry model: Estimates of seasonal to multidecadal surface ocean pCO₂ and air-sea CO₂ flux. J. Adv. Model. Earth Syst. 12, e2019MS001888 (2020).
- D. B. Chelton, M. G. Schlax, R. M. Samelson, Global observations of nonlinear mesoscale eddies. Prog. Oceanogr. 91, 167–216 (2011).
- C. Pegliasco, A. Delepoulle, E. Mason, R. Morrow, Y. Faugère, G. Dibarboure, META3.1exp: A new global mesoscale eddy trajectory atlas derived from altimetry. *Earth Syst. Sci. Data* 14, 1087–1107 (2022).
- C. Wunsch, R. Ferrari, Vertical mixing, energy, and the general circulation of the oceans. Annu. Rev. Fluid Mech. 36, 281–314 (2004).
- D. J. McGillicuddy, L. A. Anderson, N. R. Bates, T. Bibby, K. O. Buesseler, C. A. Carlson, C. S. Davis, C. Ewart, P. G. Falkowski, S. A. Goldthwait, D. A. Hansell, W. J. Jenkins, R. Johnson, V. K. Kosnyrev, J. R. Ledwell, Q. P. Li, D. A. Siegel, D. K. Steinberg, Eddy/wind interactions stimulate extraordinary mid-ocean plankton blooms. *Science* 316, 1021–1026 (2007).
- D. B. Chelton, P. Gaube, M. G. Schlax, J. J. Early, R. M. Samelson, The influence of nonlinear mesoscale eddies on near-surface oceanic chlorophyll. Science 334, 328–332 (2011).
- I. Frenger, N. Gruber, R. Knutti, M. Münnich, Imprint of Southern Ocean eddies on winds, clouds and rainfall. Nat. Geosci. 6, 608–612 (2013).
- F. Dufois, N. J. Hardman-Mountford, J. Greenwood, A. J. Richardson, M. Feng, R. J. Matear, Anticyclonic eddies are more productive than cyclonic eddies in subtropical gyres because of winter mixing. Sci. Adv. 2, e1600282 (2016).
- A. B. Villas Bôas, O. T. Sato, A. Chaigneau, G. P. Castelão, The signature of mesoscale eddies on the air-sea turbulent heat fluxes in the South Atlantic Ocean. *Geophys. Res. Lett.* 42, 1856–1862 (2015).
- H. Chen, F. A. Haumann, L. D. Talley, K. S. Johnson, J. L. Sarmiento, The deep ocean's carbon exhaust. Global Biogeochem. Cycles 36, e2021GB007156 (2022).
- E. M. Jones, M. Hoppema, V. Strass, J. Hauck, L. Salt, S. Ossebaar, C. Klaas,
 M. A. C. Van Heuven, D. Wolf-Gladrow, T. Stöven, H. J. W. De Baar, Mesoscale features

SCIENCE ADVANCES | RESEARCH ARTICLE

- create hotspots of carbon uptake in the Antarctic Circumpolar Current. *Deep Sea Res. Il Top. Stud. Oceanogr.* **138**, 39–51 (2017).
- H. Song, J. Marshall, D. R. Munro, S. Dutkiewicz, C. Sweeney, D. J. McGillicuddy Jr.,
 U. Hausmann, Mesoscale modulation of air-sea CO₂ flux in Drake Passage. J. Geophys. Res. Oceans 121, 6635–6649 (2016).
- D. J. Ford, G. H. Tilstone, J. D. Shutler, V. Kitidis, K. L. Sheen, G. Dall'Olmo, I. B. M. Orselli, Mesoscale eddies enhance the air-sea CO₂ sink in the South Atlantic Ocean. *Geophys. Res. Lett.* 50, e2022GL 102137 (2023).
- F. Chen, W.-J. Cai, C. Benitez-Nelson, Y. Wang, Sea surface pCO₂-SST relationships across a cold-core cyclonic eddy: Implications for understanding regional variability and air-sea gas exchange. Geophys. Res. Lett. 34, L10603 (2007).
- I. B. M. Orselli, R. Kerr, J. L. L. D. Azevedo, F. Galdino, M. Araujo, C. A. E. Garcia, The sea-air CO₂ net fluxes in the South Atlantic Ocean and the role played by Agulhas eddies. *Prog. Oceanogr.* 170, 40–52 (2019).
- L. P. Pezzi, R. B. De Souza, M. F. Santini, A. J. Miller, J. T. Carvalho, C. K. Parise, M. F. Quadro, E. B. Rosa, F. Justino, U. A. Sutil, M. J. Cabrera, A. V. Babanin, J. Voermans, E. L. Nascimento, R. C. M. Alves, G. B. Munchow, J. Rubert, Oceanic eddy-induced modifications to air–sea heat and CO₂ fluxes in the Brazil-Malvinas Confluence. *Sci. Rep.* 11, 10648 (2021).
- S. Moreau, A. D. Penna, J. Llort, R. Patel, C. Langlais, P. W. Boyd, R. J. Matear, H. E. Phillips, T. W. Trull, B. Tilbrook, A. Lenton, P. G. Strutton, Eddy-induced carbon transport across the Antarctic Circumpolar Current. *Global Biogeochem. Cycles* 31, 1368–1386 (2017).
- R. F. Weiss, Carbon dioxide in water and seawater: The solubility of a non-ideal gas. Mar. Chem. 2, 203–215 (1974).
- D. J. McGillicuddy, Mechanisms of physical-biological-biogeochemical interaction at the oceanic mesoscale. Ann. Rev. Mar. Sci. 8, 125–159 (2016).
- P. Gaube, D. J. McGillicuddy, D. B. Chelton, M. J. Behrenfeld, P. G. Strutton, Regional variations in the influence of mesoscale eddies on near-surface chlorophyll. J. Geophys. Res. Oceans 119, 8195–8220 (2014).
- Y. Guo, M.-L. Timmermans, The role of ocean mesoscale variability in air-sea CO₂ exchange: A global perspective. *Geophys. Res. Lett.* 51, e2024GL108373 (2024).
- L. Gregor, J. Shutler, N. Gruber, High-resolution variability of the ocean carbon sink. Global Biogeochem. Cycles 38, e2024GB008127 (2024).
- J. Ji, C. Dong, B. Zhang, Y. Liu, B. Zou, G. P. King, G. Xu, D. Chen, Oceanic eddy characteristics and generation mechanisms in the Kuroshio Extension region. *J. Geophys. Res. Oceans* 123, 8548–8567 (2018).
- Y. N. Sasaki, S. Minobe, Climatological mean features and interannual to decadal variability of ring formations in the Kuroshio Extension region. *J. Oceanogr.* 71, 499–509 (2015)
- T. Tokoro, S. Nakaoka, S. Takao, S. Saito, D. Sasano, K. Enyo, M. Ishii, N. Kosugi, Y. Nojiri, Statistical analysis of spatiotemporal variations of air-sea CO₂ fluxes in the Kuroshio region. J. Geophys. Res. Oceans 128, e2023JC019762 (2023).
- A. R. Fay, L. Gregor, P. Landschützer, G. A. McKinley, N. Gruber, M. Gehlen, Y. Iida, G. G. Laruelle, C. Rödenbeck, A. Roobaert, J. Zeng, SeaFlux: Harmonization of air–sea CO₂ fluxes from surface pCO₂ data products using a standardized approach. Earth Syst. Sci. Data 13, 4693–4710 (2021).
- O. Hoegh-Guldberg, D. Jacob, M. Taylor, M. Bindi, S. Brown, I. Camilloni, A. Diedhiou, R. Djalante, K. L. Ebi, F. Engelbrecht, J. Guiot, Y. Hijioka, S. Mehrotra, A. Payne, S. I. Seneviratne, A. Thomas, R. Warren, G. Zhou, "Global warming of 1.5°C," V. Masson-Delmotte, P. Zhai, H.-O. Pörtner, D. Roberts, J. Skea, P. R. Shukla, A. Pirani, W. Moufouma-Okia, C. Péan, R. Pidcock, S. Connors, J. B. R. Matthews, Y. Chen, X. Zhou, M. I. Gomis, E. Lonnoy, T. Maycock, M. Tignor, T. Waterfield, Eds. (2018), pp. 175–311.
- J. J. M. Busecke, R. P. Abernathey, Ocean mesoscale mixing linked to climate variability. Sci. Adv. 5, eaav5014 (2019).
- S. T. Cole, C. Wortham, E. Kunze, W. B. Owens, Eddy stirring and horizontal diffusivity from Argo float observations: Geographic and depth variability. *Geophys. Res. Lett.* 42, 3989–3997 (2015).
- 41. Y. Lehahn, F. d'Ovidio, M. Lévy, Y. Amitai, E. Heifetz, Long range transport of a quasi isolated chlorophyll patch by an Agulhas ring, *Geophys. Res. Lett.* **38**, (2011).
- X. Wang, Y. Du, Y. Zhang, A. Wang, T. Wang, Influence of two eddy pairs on high-salinity water intrusion in the Northern South China Sea during fall-winter 2015/2016. J. Geophys. Res. Oceans 126, e2020JC016733 (2021).
- P. Gaube, D. B. Chelton, P. G. Strutton, M. J. Behrenfeld, Satellite observations of chlorophyll, phytoplankton biomass, and Ekman pumping in nonlinear mesoscale eddies. J. Geophys. Res. Oceans 118, 6349–6370 (2013).
- P. Gaube, D. B. Chelton, R. M. Samelson, M. G. Schlax, L. W. O'Neill, Satellite observations of mesoscale eddy-induced Ekman pumping. *J. Phys. Oceanogr.* 45, 104–132 (2015).
- D. A. Siegel, P. Peterson, D. J. McGillicuddy, S. Maritorena, N. B. Nelson, Bio-optical footprints created by mesoscale eddies in the Sargasso Sea. *Geophys. Res. Lett.* 38, L13608 (2011)
- P. G. Falkowski, D. Ziemann, Z. Kolber, P. K. Bienfang, Role of eddy pumping in enhancing primary production in the ocean. *Nature* 352, 55–58 (1991).

- P. Klein, G. Lapeyre, The oceanic vertical pump induced by mesoscale and submesoscale turbulence. Ann. Rev. Mar. Sci. 1, 351–375 (2009).
- D. Kim, S.-E. Lee, S. Cho, D.-J. Kang, G.-H. Park, S. K. Kang, Mesoscale eddy effects on sea-air CO₂ fluxes in the northern Philippine Sea. Front. Mar. Sci. 9, 970678 (2022).
- P. Gaube, D. J. McGillicuddy, A. J. Moulin, Mesoscale eddies modulate mixed layer depth globally. Geophys. Res. Lett. 46, 1505–1512 (2019).
- A. R. Fay, G. A. McKinley, Correlations of surface ocean pCO₂ to satellite chlorophyll on monthly to interannual timescales. *Global Biogeochem. Cycles* 31, 436–455 (2017).
- J. Huang, F. Xu, K. Zhou, P. Xiu, Y. Lin, Temporal evolution of near-surface chlorophyll over cyclonic eddy lifecycles in the southeastern Pacific. *J. Geophys. Res. Oceans* 122, 6165–6179 (2017).
- Q. He, H. Zhan, S. Cai, Z. Li, Eddy effects on surface chlorophyll in the northern South China Sea: Mechanism investigation and temporal variability analysis. *Deep Sea Res. Part Oceanogr. Res. Pap.* 112, 25–36 (2016).
- Q. Liu, Y. Liu, X. Li, Characteristics of surface physical and biogeochemical parameters within mesoscale eddies in the Southern Ocean. *Biogeosciences* 20, 4857–4874 (2023).
- Y. Wang, R. Bi, J. Zhang, J. Gao, S. Takeda, Y. Kondo, F. Chen, G. Jin, J. P. Sachs, M. Zhao, Phytoplankton distributions in the Kuroshio-Oyashio region of the Northwest Pacific Ocean: Implications for marine ecology and carbon cycle. Front. Mar. Sci. 9, 865142 (2022).
- Y. Wang, J. Kang, X. Sun, J. Huang, Y. Lin, P. Xiang, Spatial patterns of phytoplankton community and biomass along the Kuroshio Extension and adjacent waters in late spring. *Mar. Biol.* 168, 40 (2021).
- L. Resplandy, M. Lévy, D. J. McGillicuddy, Effects of eddy-driven subduction on ocean biological carbon pump. Global Biogeochem. Cycles 33, 1071–1084 (2019).
- IEA, "CO2 Emissions in 2022" (IEA, Paris, 2023); www.iea.org/reports/co2-emissionsin-2022
- J. Martínez-Moreno, A. McC, M. H. Hogg, N. C. England, A. E. Constantinou, A. K. Kiss, A. D. Morrison, Global changes in oceanic mesoscale currents over the satellite altimetry record. *Nat. Clim. Chang.* 11, 397–403 (2021).
- N. Beech, T. Rackow, T. Semmler, S. Danilov, Q. Wang, T. Jung, Long-term evolution of ocean eddy activity in a warming world. Nat. Clim. Chang. 12, 910–917 (2022).
- D. Couespel, M. Lévy, L. Bopp, Stronger oceanic CO₂ sink in eddy-resolving simulations of global warming. Geophys. Res. Lett. 51, e2023GL106172 (2024).
- 61. S. Sathyendranath, R. J. W. Brewin, C. Brockmann, V. Brotas, B. Calton, A. Chuprin, P. Cipollini, A. B. Couto, J. Dingle, R. Doerffer, C. Donlon, M. Dowell, A. Farman, M. Grant, S. Groom, A. Horseman, T. Jackson, H. Krasemann, S. Lavender, V. Martinez-Vicente, C. Mazeran, F. Mélin, T. S. Moore, D. Müller, P. Regner, S. Roy, C. J. Steele, F. Steinmetz, J. Swinton, M. Taberner, A. Thompson, A. Valente, M. Zühlke, V. E. Brando, H. Feng, G. Feldman, B. A. Franz, R. Frouin, R. W. Gould, S. B. Hooker, M. Kahru, S. Kratzer, B. G. Mitchell, F. E. Muller-Karger, H. M. Sosik, K. J. Voss, J. Werdell, T. Platt, An ocean-colour time series for use in climate studies: The experience of the Ocean-Colour Climate Change Initiative (OC-CCI). Sensors 19, 4285 (2019).
- NASA/JPL, "MODIS Aqua Level 3 SST Thermal IR Daily 4km Daytime V2019.0" (NASA Physical Oceanography Distributed Active Archive Center, 2020); https://doi.org/10.5067/ MODSA-1D4D9.
- NASA/OBPG, "MODIS Aqua Level 3 Mapped Photosynthetically Available Radiation Data, Version R2022.0" (NASA Ocean Biology Distributed Active Archive Center, 2022); https://oceancolor.gsfc.nasa.gov/data/10.5067/AQUA/MODIS/L3M/PAR/2022.0/.
- A. Morel, Light and marine photosynthesis: A spectral model with geochemical and climatological implications. *Prog. Oceanogr.* 26, 263–306 (1991).
- CMEMS, "Global Ocean Gridded L4 Sea Surface Heights And Derived Variables Reprocessed 1993 Ongoing" (CMEMS Marine Data Store, 2023); https://doi.org/10.48670/moi-00148.
- H. Yang, B. Qiu, P. Chang, L. Wu, S. Wang, Z. Chen, Y. Yang, Decadal variability of eddy characteristics and energetics in the Kuroshio Extension: Unstable versus stable states. J. Geophys. Res. Oceans 123, 6653–6669 (2018).
- CMEMS, "Global Ocean Physics Reanalysis" (Marine Data Store, 2023); https://doi. org/10.48670/moi-00021.
- B. Pfeil, A. Olsen, D. C. E. Bakker, S. Hankin, H. Koyuk, A. Kozyr, J. Malczyk, A. Manke, N. Metzl, C. L. Sabine, J. Akl, S. R. Alin, N. Bates, R. G. J. Bellerby, A. Borges, J. Boutin, P. J. Brown, W.-J. Cai, F. P. Chavez, A. Chen, C. Cosca, A. J. Fassbender, R. A. Feely, M. González-Dávila, C. Goyet, B. Hales, N. Hardman-Mountford, C. Heinze, M. Hood, M. Hoppema, C. W. Hunt, D. Hydes, M. Ishii, T. Johannessen, S. D. Jones, R. M. Key, A. Körtzinger, P. Landschützer, S. K. Lauvset, N. Lefèvre, A. Lenton, A. Lourantou, L. Merlivat, T. Midorikawa, L. Mintrop, C. Miyazaki, A. Murata, A. Nakadate, Y. Nakano, S. Nakaoka, Y. Nojiri, A. M. Omar, X. A. Padin, G.-H. Park, K. Paterson, F. F. Perez, D. Pierrot, A. Poisson, A. F. Ríos, J. M. Santana-Casiano, J. Salisbury, V. V. S. S. Sarma, R. Schlitzer, B. Schneider, U. Schuster, R. Sieger, I. Skjelvan, T. Steinhoff, T. Suzuki, T. Takahashi, K. Tedesco, M. Telszewski, H. Thomas, B. Tilbrook, J. Tjiputra, D. Vandemark, T. Veness, R. Wanninkhof, A. J. Watson, R. Weiss, C. S. Wong, H. Yoshikawa-Inoue, A uniform, quality controlled Surface Ocean CO₂ Atlas (SOCAT). Earth Syst. Sci. Data 5, 125–143 (2013).

 D. J. Ford, G. H. Tilstone, J. D. Shutler, V. Kitidis, Derivation of seawater pCO₂ from net community production identifies the South Atlantic Ocean as a CO₂ source. Biogeosciences 19. 93–115 (2022).

SCIENCE ADVANCES | RESEARCH ARTICLE

- D. K. Woolf, P. E. Land, J. D. Shutler, L. M. Goddijn-Murphy, C. J. Donlon, On the calculation of air-sea fluxes of CO₂ in the presence of temperature and salinity gradients. *J. Geophys. Res. Oceans* 121, 1229–1248 (2016).
- B. Huang, C. Liu, V. Banzon, E. Freeman, G. Graham, B. Hankins, T. Smith, H.-M. Zhang, Improvements of the Daily Optimum Interpolation Sea Surface Temperature (DOISST) version 2.1. J. Climate 34, 2923–2939 (2021).
- C. L. Sabine, S. Hankin, H. Koyuk, D. C. E. Bakker, B. Pfeil, A. Olsen, N. Metzl, A. Kozyr,
 A. Fassbender, A. Manke, J. Malczyk, J. Akl, S. R. Alin, R. G. J. Bellerby, A. Borges, J. Boutin,
 P. J. Brown, W.-J. Cai, F. P. Chavez, A. Chen, C. Cosca, R. A. Feely, M. González-Dávila,
 C. Goyet, N. Hardman-Mountford, C. Heinze, M. Hoppema, C. W. Hunt, D. Hydes, M. Ishii,
 T. Johannessen, R. M. Key, A. Körtzinger, P. Landschützer, S. K. Lauvset, N. Lefèvre,
 A. Lenton, A. Lourantou, L. Merlivat, T. Midorikawa, L. Mintrop, C. Miyazaki, A. Murata,
 A. Nakadate, Y. Nakano, S. Nakaoka, Y. Nojiri, A. M. Omar, X. A. Padin, G.-H. Park,
 K. Paterson, F. F. Perez, D. Pierrot, A. Poisson, A. F. Ríos, J. Salisbury, J. M. Santana-Casiano,
 V. V. S. S. Sarma, R. Schlitzer, B. Schneider, U. Schuster, R. Sieger, I. Skjelvan, T. Steinhoff,
 T. Suzuki, T. Takahashi, K. Tedesco, M. Telszewski, H. Thomas, B. Tilbrook, D. Vandemark,
 T. Veness, A. J. Watson, R. Weiss, C. S. Wong, H. Yoshikawa-Inoue, Surface Ocean CO₂ Atlas
 (SOCAT) gridded data products. *Earth Syst. Sci. Data* 5, 145–153 (2013).
- D. C. E. Bakker, B. Pfeil, C. S. Landa, N. Metzl, K. M. O'Brien, A. Olsen, K. Smith, C. Cosca, S. Harasawa, S. D. Jones, S. Nakaoka, Y. Nojiri, U. Schuster, T. Steinhoff, C. Sweeney, T. Takahashi, B. Tilbrook, C. Wada, R. Wanninkhof, S. R. Alin, C. F. Balestrini, L. Barbero, N. R. Bates, A. A. Bianchi, F. Bonou, J. Boutin, Y. Bozec, E. F. Burger, W.-J. Cai, R. D. Castle, L. Chen, M. Chierici, K. Currie, W. Evans, C. Featherstone, R. A. Feely, A. Fransson, C. Goyet, N. Greenwood, L. Gregor, S. Hankin, N. J. Hardman-Mountford, J. Harlay, J. Hauck, M. Hoppema, M. P. Humphreys, C. W. Hunt, B. Huss, J. S. P. Ibánhez, T. Johannessen, R. Keeling, V. Kitidis, A. Körtzinger, A. Kozyr, E. Krasakopoulou, A. Kuwata, P. Landschützer, S. K. Lauvset, N. Lefèvre, C. Lo Monaco, A. Manke, J. T. Mathis, L. Merlivat, F. J. Millero, P. M. S. Monteiro, D. R. Munro, A. Murata, T. Newberger, A. M. Omar, T. Ono, K. Paterson, D. Pearce, D. Pierrot, L. L. Robbins, S. Saito, J. Salisbury, R. Schlitzer, B. Schneider, R. Schweitzer, R. Sieger, I. Skjelvan, K. F. Sullivan, S. C. Sutherland, A. J. Sutton, K. Tadokoro, M. Telszewski, M. Tuma, S. M. A. C. Van Heuven, D. Vandemark, B. Ward, A. J. Watson, S. Xu, A multi-decade record of high-quality fCO₂ data in version 3 of the Surface Ocean CO₂ Atlas (SOCAT). Earth Syst. Sci. Data 8, 383–413 (2016).
- L. M. Goddijn-Murphy, D. K. Woolf, P. E. Land, J. D. Shutler, C. Donlon, The OceanFlux Greenhouse Gases methodology for deriving a sea surface climatology of CO₂ fugacity in support of air–Sea gas flux studies. *Ocean Sci.* 11, 519–541 (2015).
- T. Holding, I. G. Ashton, J. D. Shutler, P. E. Land, P. D. Nightingale, A. P. Rees, I. Brown, J.-F. Piolle, A. Kock, H. W. Bange, D. K. Woolf, L. Goddijn-Murphy, R. Pereira, F. Paul, F. Girard-Ardhuin, B. Chapron, G. Rehder, F. Ardhuin, C. J. Donlon, The FluxEngine air–sea gas flux toolbox: Simplified interface and extensions for in situ analyses and multiple sparingly soluble gases. *Ocean Sci.* 15, 1707–1728 (2019).
- J. D. Shutler, P. E. Land, J.-F. Piolle, D. K. Woolf, L. Goddijn-Murphy, F. Paul,
 F. Girard-Ardhuin, B. Chapron, C. J. Donlon, FluxEngine: A flexible processing system for
 calculating atmosphere—Ocean carbon dioxide gas fluxes and climatologies. J. Atmos.
 Oceanic Tech. 33, 741–756 (2016).
- P. Landschützer, N. Gruber, D. C. E. Bakker, U. Schuster, S. Nakaoka, M. R. Payne, T. P. Sasse, J. Zeng, A neural network-based estimate of the seasonal to inter-annual variability of the Atlantic Ocean carbon sink. *Biogeosciences* 10, 7793–7815 (2013).
- T.T.T. Chau, M. Gehlen, F. Chevallier, A seamless ensemble-based reconstruction of surface ocean pCO₂ and air–sea CO₂ fluxes over the global coastal and open oceans. Biogeosciences 19, 1087–1109 (2022).
- C. Rödenbeck, D. C. E. Bakker, N. Metzl, A. Olsen, C. Sabine, N. Cassar, F. Reum, R. F. Keeling, M. Heimann, Interannual sea–air CO₂ flux variability from an observationdriven ocean mixed-layer scheme. *Biogeosciences* 11, 4599–4613 (2014).
- L. Gregor, A. D. Lebehot, S. Kok, P. M. Scheel Monteiro, A comparative assessment of the uncertainties of global surface ocean CO₂ estimates using a machine-learning ensemble (CSIR-ML6 version 2019a) – Have we hit the wall? *Geosci. Model Dev.* 12, 5113–5136 (2019).
- J. Zeng, Y. Nojiri, P. Landschützer, M. Telszewski, S. Nakaoka, A global surface ocean fCO₂ climatology based on a feed-forward neural network. *J. Atmospheric Ocean. Technol.* 31, 1838–1849 (2014).
- G. Zhong, X. Li, J. Song, B. Qu, F. Wang, Y. Wang, B. Zhang, X. Sun, W. Zhang, Z. Wang, J. Ma, H. Yuan, L. Duan, Reconstruction of global surface ocean pCO₂ using region-specific predictors based on a stepwise FFNN regression algorithm. *Biogeosciences* 19, 845–859 (2022).
- A. Longhurst, S. Sathyendranath, T. Platt, C. Caverhill, An estimate of global primary production in the ocean from satellite radiometer data. *J. Plankton Res.* 17, 1245–1271 (1995).

- R. Wanninkhof, Relationship between wind speed and gas exchange over the ocean revisited: Gas exchange and wind speed over the ocean. *Limnol. Oceanogr. Methods* 12, 351–362 (2014).
- C. J. Donlon, P. J. Minnett, C. Gentemann, T. J. Nightingale, I. J. Barton, B. Ward,
 M. J. Murray, Toward improved validation of satellite sea surface skin temperature measurements for climate research. J. Climate 15, 353–369 (2002).
- A. J. Watson, U. Schuster, J. D. Shutler, T. Holding, I. G. C. Ashton, P. Landschützer,
 D. K. Woolf, L. Goddijn-Murphy, Revised estimates of ocean-atmosphere CO₂ flux are consistent with ocean carbon inventory. *Nat. Commun.* 11, 4422 (2020).
- N. S. Lovenduski, N. Gruber, S. C. Doney, I. D. Lima, Enhanced CO₂ outgassing in the Southern Ocean from a positive phase of the Southern Annular Mode. *Global Biogeochem. Cycles* 21, GB2026 (2007).
- E. Liao, L. Resplandy, J. Liu, K. W. Bowman, Amplification of the ocean carbon sink during El Niños: Role of poleward Ekman transport and influence on atmospheric CO₂. Global Biogeochem. Cycles 34, e2020GB006574 (2020).
- 90. J. L. Sarmiento, Ocean Biogeochemical Dynamics (Princeton University Press, 2006).
- K. Lee, L. T. Tong, F. J. Millero, C. L. Sabine, A. G. Dickson, C. Goyet, G.-H. Park, R. Wanninkhof, R. A. Feely, R. M. Key, Global relationships of total alkalinity with salinity and temperature in surface waters of the world's oceans. *Geophys. Res. Lett.* 33, 2006GL027207 (2006).
- J. D. Sharp, D. Pierrot, M. P. Humphreys, J.-M. Epitalon, J. C. Orr, E. R. Lewis,
 D. W. R. Wallace, CO2SYSv3 for MATLAB, version v3.2.1 (2023); https://doi.org/10.5281/zenodo.7552554.
- T. J. Lueker, A. G. Dickson, C. D. Keeling, Ocean pCO₂ calculated from dissolved inorganic carbon, alkalinity, and equations for K₁ and K₂: Validation based on laboratory measurements of CO₂ in gas and seawater at equilibrium. Mar. Chem. 70, 105–119 (2000).
- 94. A. G. Dickson, Standard potential of the reaction: $AgCl(s) + 1/2H_2(g) = Ag(s) + HCl(aq)$, and the standard acidity constant of the ion HSO_4^- in synthetic sea water from 273.15 to 318.15 K. *J. Chem. Thermodyn.* **22**, 113–127 (1990).
- K. Lee, T.-W. Kim, R. H. Byrne, F. J. Millero, R. A. Feely, Y.-M. Liu, The universal ratio of boron to chlorinity for the North Pacific and North Atlantic oceans. *Geochim. Cosmochim. Acta* 74, 1801–1811 (2010).
- D. Ford, G. H. Tilstone, J. D. Shutler, V. Kitidis, P. Lobanova, J. Schwarz, A. J. Poulton, P. Serret, T. Lamont, M. Chuqui, R. Barlow, J. Lozano, M. Kampel, F. Brandini, Wind speed and mesoscale features drive net autotrophy in the South Atlantic Ocean. *Remote Sens. Environ.* 260, 112435 (2021).
- M. Drévillon, J.-M. Lellouche, C. Régnier, G. Garric, C. Bricaud, O. Hernandez, R. Bourdallé-Badie, "Quality information document for products GLOBAL_ REANALYSIS_PHY_001_030" (EU Copernicus Marine Service, 2023); https://catalogue.marine.copernicus.eu/documents/QUID/CMEMS-GLO-QUID-001-030.pdf.
- D. K. Woolf, J. D. Shutler, L. Goddijn-Murphy, A. J. Watson, B. Chapron, P. D. Nightingale, C. J. Donlon, J. Piskozub, M. J. Yelland, I. Ashton, T. Holding, U. Schuster, F. Girard-Ardhuin, A. Grouazel, J.-F. Piolle, M. Warren, I. Wrobel-Niedzwiecka, P. E. Land, R. Torres, J. Prytherch, B. Moat, J. Hanafin, F. Ardhuin, F. Paul, Key uncertainties in the recent air-sea flux of CO₂. Global Biogeochem. Cycles 33, 1548–1563 (2019).
- Y. Iida, Y. Takatani, A. Kojima, M. Ishii, Global trends of ocean CO₂ sink and ocean acidification: An observation-based reconstruction of surface ocean inorganic carbon variables. J. Oceanogr. 77, 323–358 (2021).

Acknowledgments: We are grateful to all the researchers and funding agencies who have contributed to SOCAT. We thank the anonymous reviewers for constructive comments, which have helped improve the manuscript, Funding: This study was funded by the National Natural Science Foundation of China (92258302 to B.G. and Z.Ca., 42276016 to B.G., 42225601 to Z.Ch., and 42288101 to Z.Z.). Author contributions: Conceptualization: B.G., B.Q., and L.W Methodology: X.L., B.G., and Z.Z. Formal analysis: X.L. and B.G. Visualization: X.L. and B.G. Validation: X.L., B.G., and Z.Z. Funding acquisition: B.G., Z.Ca., Z.Z., and Z.Ch. Writing—original draft: X.L., B.G., and B.Q. Writing-review and editing: B.G., X.L., Z.Z., Z.Ca., B.Q., Z.Ch., and L.W. Competing interests: The authors declare that they have no competing interests. Data and materials availability: All data needed to evaluate the conclusions in the paper are present in the paper and/or the Supplementary Materials. OC-CCI ChI a data are publicly available from https://climate.esa.int/en/projects/ocean-colour/. MODIS-A SST and PAR data can be downloaded from https://oceancolor.gsfc.nasa.gov/. NOAA OISST data are available from $https://psl.noaa.gov/data/gridded/data.noaa.oisst.v2.highres.html.\ Altimeter\ SSHA\ and$ geostrophic velocity data can be downloaded from https://data.marine.copernicus.eu/ product/SEALEVEL_GLO_PHY_L4_MY_008_047. CMEMS SSS and MLD data are available from https://data.marine.copernicus.eu/product/GLOBAL_MULTIYEAR_PHY_001_030, CCMP wind product data are available from www.remss.com/measurements/ccmp/. SOCAT version 2022 data are publicly available from https://socat.info/index.php/data-access/. Atmospheric pCO₂

SCIENCE ADVANCES | RESEARCH ARTICLE

data are publicly available from www.ncei.noaa.gov/access/metadata/landing-page/bin/iso?id=gov.noaa.nodc:0160558. SeaFlux sea-air FCO2 data are publicly available from https://zenodo.org/records/5482547. Global mesoscale eddy trajectory data (META3.2 DT) are publicly available from www.aviso.altimetry.fr/en/data/products/value-added-products/global-mesoscale-eddy-trajectory-product.html. The DIC data from JMA-MLR can be downloaded from www.data.jma.go.jp/gmd/kaiyou/english/co2_flux/co2_flux_data_en.html. CO2SYS for Matlab version 3.2.1 can be accessed from https://zenodo.org/records/7552554. The

FluxEngine code, as well as the data and analysis code used to generate the figures in this paper, is available at https://zenodo.org/records/15283399.

Submitted 26 September 2024 Accepted 6 May 2025 Published 11 June 2025 10.1126/sciadv.adt4195